Wind and Structures, *Vol. 25, No. 2 (2017) 177-193*
DOI: https://doi.org/10.12989/was.2017.25.2.177

Computational study of the wind load on a free-form complex thin shell structure

A. Moret Rodrigues*, Ana Tomé[a] and M. Glória Gomes[b]

CEris, ICIST, Department of Civil Engineering, Architecture and Georesources, Instituto Superior Técnico, Universidade de Lisboa, Av. Rovisco Pais 1049-001 Lisbon, Portugal

(Received April 20, 2017, Revised July 11, 2017, Accepted July 14, 2017)

Abstract. The accelerated development of new materials, technologies and construction processes, in parallel with advances in computational algorithms and ever growing computational power, is leading to more daring and innovative architectural and structural designs. The search for non-regular building shapes and slender structures, as alternative to the traditional architectural forms that have been prevailing in the building sector, poses important engineering challenges in the assessment of the strength and mechanical stability of non-conventional structures and systems, namely against highly variable actions as wind and seismic forces. In case of complex structures, laboratory experiments are a widely used methodology for strength assessment and loading characterization. Nevertheless, powerful numerical tools providing reliable results are also available today and able to compete with the experimental approach. In this paper the wind action on a free-form complex thin shell is investigated through 3D-CFD simulation in terms of the pressure coefficients and global forces generated. All the modelling aspects and calibrating process are described. The results obtained showed that the CFD technique is effective in the study of the wind effects on complex-shaped structures.

Keywords: free-form shell; wind load; pressure coefficients; global forces; CFD simulation

1. Introduction

The size and robustness of buildings in ancient times were dictated by the strength of natural materials and by the weights and dimensions that could be handled within the limits of human power and available technology. Building design and safety assessment were mainly based on empirical rules because structural behaviour was not clearly understood from a scientific point of view. Usually, the entire projects were taken in charge, from design to construction, by master builders, who were recognized to possess the body of knowledge of the design and construction practice. The knowledge was based on accumulated experience from previous projects and building works and the set of rules and procedures were deduced empirically from the observation of existing buildings. With the development of materials science and structural analysis, together with the probabilistic theory, building design and structural safety began to be conducted through a

*Corresponding author, Professor, E-mail: moret.rodrigues@tecnico.ulisboa.pt
[a] Professor, Email: anatome@tecnico.ulisboa.pt
[b] Professor, Email: maria.gloria.gomes@tecnico.ulisboa.pt

http://www.techno-press.org/?journal=was&subpage=8 ISSN: 1226-6116 (Print), 1598-6225 (Online)

scientific approach, which allowed for more well-founded and reliable safety estimations.

Following the great progress on structural engineering, regarding either numerical calculation or experimental analysis, the development of computational tools and the advancements in building technologies and construction materials have enabled the design of more slender and lighter structures, aesthetically more appealing and economically more advantageous. In what concerns the architectural design, the building sector, contrarily to the nautical, automobile and aeroplane industries, has been dominated by an architecture based on simple, geometrical forms, involving lines, two-dimensional figures and regular polyhedrons combined with spheres, ellipses and circles. In recent years, the advances in new materials (high performance steel, ultra-high performance fibre concrete, fibre reinforced polymers, other materials), quality control assessment and geometry-defining software have made it possible to increase the scale of structures and develop innovative designs and more complex forms involving free-form shapes (Rogers 2009). The design of complex shaped structures is not a current problem and poses relevant engineering challenges, particularly regarding structural safety and stability under the expected design loads. The problem can be stated in terms of the definition of the static and dynamic loads acting on the structure, on one hand, and the calculation model to predict the structural response to these loads, on the other hand. Wind is one of the significant forces of nature that must be considered in the design of building structures. Traditionally, the prediction of the wind effects on buildings and structures was carried out through wind tunnel experiments, where air is blown across a scaled model and the generated surface pressure field measured (Peterka 1983, Bienkiewicz and Sun 1992, Gomes *et al.* 2005, Zisis and Stathopoulos 2009, Amin and Ahuja 2011). Nowadays, with the computational advances, powerful CFD tools constitute an attractive alternative to the use of wind tunnel tests (Murakami and Mochida 1988, Baskaran and Kashef 1996, Liu *et al.* 2010, Montazeri and Blocken 2013). An extensive review of CFD applications in building performance simulation for the outdoor environment, including computational modelling of wind flow around buildings, was done by Blocken *et al.* (2011). Most of the works quoted in this review are addressed to regular building shapes and discussion of turbulence models performance. The present paper also deals with the application of CFD in wind engineering and turbulence modelling but, instead of focusing on regular buildings, the emphasis is on a complex-shaped thin shell structure, for which the arisen flow patterns and the corresponding load effects are investigated. It should be mentioned that the investigated shell combines an aesthetic and structural design suitable to be used as a large-span space enclosure, which makes it a very interesting case study. The shape was generated through the Rhino 3D software (McNeel and Associates 2003) and the ANSYS Fluent package (ANSYS Fluent 2012) has been the tool used to perform the CFD simulations. The details of the problem studied are given in the next sections.

2. Description of the computational problem

Thin shell structures are engineering solutions designed to economically cover large spans for industrial, commercial, and public structures. Moreover, they render an aesthetic expression much appreciated from an architectural point of view. These structures have been receiving increasing attention in recent years, due to the advances in concrete technology and computational tools for structural analysis. The problem studied in this paper is a thin shell structure in high-strength concrete with a shape optimized in terms of load transfer capabilities and performance. As an optimal structural design implies a compression-only form, the configuration of the shell was

generated through a form-finding method, specifically the force density method (Vizotto and Ferreira 2015, Adriaenssens *et al.* 2014). A very complete description of the process for obtaining the shell, including the fabric framework and involved costs, can be found in Tomé *et al.* (2014). The geometry of the structure, which was implemented in full-scale in the CFD model, is sketched in Fig. 1, with *H* and *L* approximately equal to 8 m and 23 m, respectively.

The geometry is highly irregular – in the sense that cannot be represented by classical geometry – and falls outside the typical structures for which generic rules for computational domain sizing, based on wind tunnel experiments, are available in the literature. The boundaries of the computational domain should be sufficiently far from the region where the structure is placed, which implies that the dimensions of the overall simulation volume should be matter of concern.

Although these dimensions in numerical studies on airflow around buildings may vary with the problem type and between authors, for the single building model some guidelines for a general practise have been proposed (Franke *et al.* 2007). Stated briefly, to eliminate the flow obstacle effect on the simulation volume boundaries, the recommendations for the minimum distances from the building surfaces to the volume boundaries are: *5H* between the roof and the top boundary, *5H* between the sidewalls and respective lateral boundaries, *5H* between the windward façade and the inflow boundary and *15H* between the leeward façade and the outflow boundary, where *H* is the building height.

The case under study consists of a thin shell structure, with no significant surface area opposing to the wind direction (low wind tunnel blockage ratio). The disturbance introduced in the flow by this slender open structure should be of relatively lower extent than that of a rectangular building with the same characteristic height. For this reason, the relationships between the domain dimensions and the structure height could certainly be smaller than those prescribed above. Nevertheless, in the absence of more reliable criteria, they were adopted in this study, leading to a computational domain with dimensions scaled accordingly for the length, width and height directions, as shown in Fig. 2.

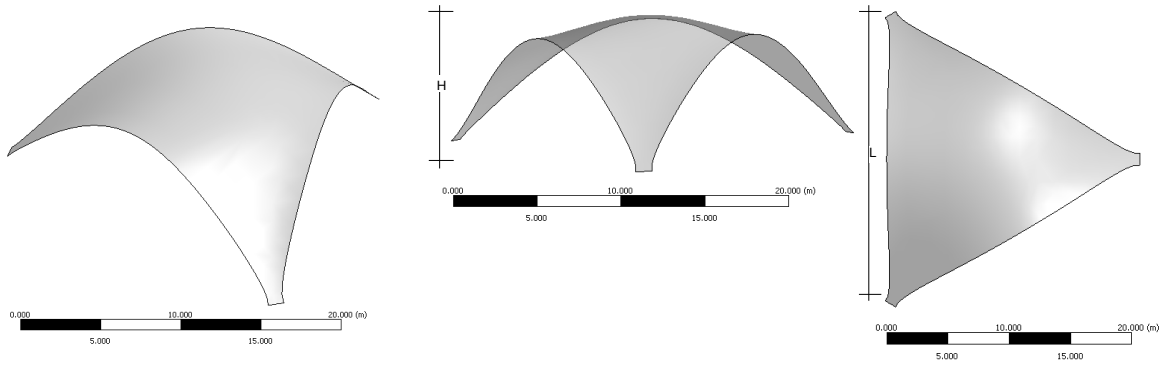

(a) isometric-view (b) front-view (c) top-view

Fig. 1 Shell structure

The characteristics of the studied model did not allow the use of a structured grid over the entire domain. In this way, a hybrid grid basically structured into two regions was adopted for the spatial discretization of the computational domain: an inner region surrounding the model, where an unstructured grid, primarily composed of tetrahedral elements, was applied; and the rest of the domain, where a structured grid essentially composed of quadrangular prisms was generated. Some samples of the computational grid are shown in Fig. 3, evidencing the three main parts of the domain: upstream, central and downstream parts.

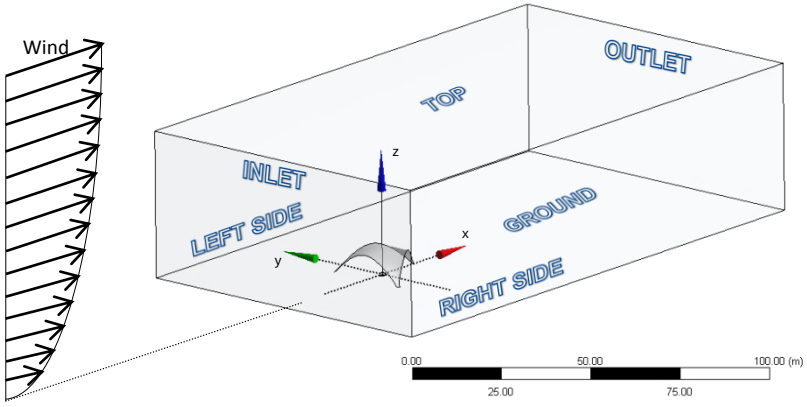

Fig. 2 Shell structure and calculation domain

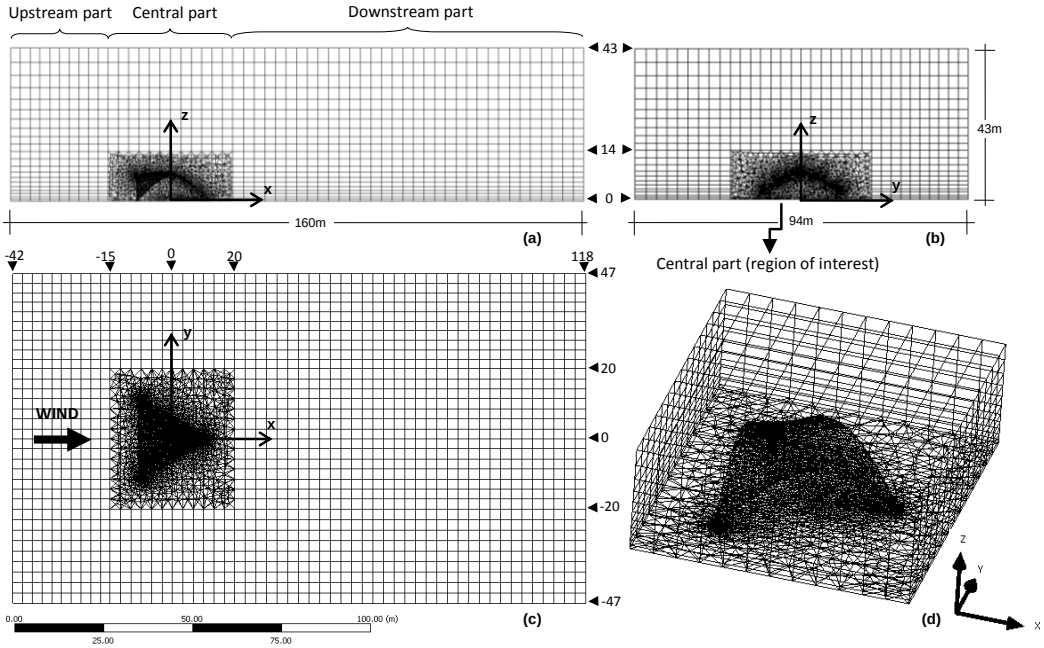

Fig. 3 Computational grid: (a) side view, (b) front view, (c) top view and (d) central part

Near the ground and solid surfaces the grid was refined through a stretching ratio on mesh resolution to capture the steep gradients of the flow variables. The skewness and aspect ratio of cells were also checked to prevent numerical instabilities and assure a good description of the flow. The control-volume-based technique (finite volume discretization process) and the pressure-based segregated algorithm of FLUENT were used to solve the equations for conservation of mass and momentum, in conjunction with a k-ε turbulence model, as discussed in the next section. The second-order upwind scheme was applied for the convective terms of the governing equations, and the SIMPLE algorithm was used for pressure-velocity coupling.

3. Turbulence modelling

A variety of models are currently available in CFD software packages to simulate turbulence flows and can be classified into three main categories: Direct Numerical Simulation (DNS), Large Eddy Simulation (LES) and Reynolds-Averaged Navier-Stokes (RANS) simulation. The first two categories are claimed to provide accurate predictions of the flow but have the drawback of being too computationally expensive to be used in engineering problems. In fact, both approaches require huge grid densities to capture the smallest scales of motion, which may not be feasible with computer memory and runtime speed. RANS models perform well boundary layers and require considerably less computer resources than DNS or LES. Among the RANS models, the two equations k-ε turbulence model is the most common model employed to simulate mean flow characteristics for turbulent flow conditions. The standard version of this model, due to its robustness, simplicity and realistic predictions, is indubitably the most widely used and validated turbulence modelling method for engineering problems. Nevertheless, it has been reported to perform poorly in case of curved boundary layers, low Reynolds number flows, and recirculating flows, especially near the separation and reattachment points. To improve the model predictions, revised versions of the standard k-ε model (SKE) – KL model and MMK model – and other modified versions – RNG and Realizable k-ε (RKE) models – have been proposed. Although these variants of the standard k-ε model produce improved results, each performs better in certain problems than others, depending on the geometry and physics of the particular application. In wind engineering applications, the uni-directional atmospheric boundary layer flow undergoes a sudden change in direction when encounters an obstacle, giving rise to zones of increased pressure (windward side) and others of low and negative pressure (suction), which result in flow separation and formation of recirculation regions, where the flow velocities are low (leeward and lateral sides). Studies on this problem, comparing the performance of different turbulent models, are very common in the literature (Behrouzi *et al*. 2013, Irtaza *et al*. 2013, Liu *et al.* 2013, Yazid *et al.* 2013, Evola and Popov 2006). Focusing on the application of the SKE, RNG k-ε and RKE models to the wind flow around a building, Behrouzi *et al.* (2013) reported that the reattachment length on the roof is not predicted by the SKE model and that the RNG k-ε and RKE models have a good agreement with experimental data. In another study, Irtaza *et al.* (2013) compared the wind tunnel experiments on a scaled real building with CFD simulations and concluded that the accuracy of the calculated pressure coefficients is not the same at all sides of the building, with the RNG k-ε and the RKE models showing a similar performance that globally is higher than the SKE model. Similar conclusions were drawn by Liu *et al.* (2013) for the wind induced surface pressures on a complex-shaped building, with the SKE model over-predicting the pressure values compared to

the RNG k-ε and the RKE models. In other wind related subjects, such as wind flows in canyons, pollutant dispersion and building ventilation, it also has been demonstrated the superior performance of the RNG k-ε and the RKE models compared with the SKE model (Yazid *et al.* 2013, Lateb *et al.* 2010, Evola and Popov 2006).

The RNG k-ε model, giving its relatively large acceptance in research and studies of wind effects on buildings, was selected in this work to model the turbulence phenomena induced by the ground and shell surfaces and its subsequent influence on the fluid flow features. The RNG k-ε model is derived from the instantaneous Navier-Stokes equations using a rigorous statistical technique, called renormalized group method, to account for the effects of smaller scales of motion. The model is similar to the standard k-ε model but has different constants and additional terms and functions in the turbulent kinetic energy (k) and turbulent dissipation (ε) transport equations (Yakhot *et al.* 1992).

To resolve the flow near the solid surfaces – in the present case, the shell and ground surfaces – without the expense of exaggerated simulation time and computational memory, the wall functions method was used. Wall functions consist of empirical formulae and functions to link the dependent variables at the near-wall cells to the corresponding parameters on the wall. The mean velocity and temperature (in cases wherein heat transfer is present) are determined through functions composed of laws-of-the-wall of logarithmic base lying on the hypothesis of constant shear stress – and equal to the wall shear stress – in the region adjacent to the wall. The near-wall turbulent quantities are directly computed through corresponding formulae, which are derived, in the case of the standard version of the method, from the assumption of local equilibrium of turbulence (production rate of k equals its dissipation rate) and consistent with the use of the logarithmic law of the wall. The laws-of-the-wall are normally addressed to hydraulically smooth surfaces. In case of rough surfaces, the laws-of-the-wall are modified to incorporate the so called roughness shift, which represents the vertical displacement between the smooth-wall and rough-wall velocity profiles on a semi-logarithmic plot. For the k-ε model, the standard wall functions and the non-equilibrium wall functions are options of the wall functions method that are usually available in current CFD packages. Although the former have been more intensively used in engineering applications and give reasonably accurate predictions for high-Reynolds-number flows with small pressure gradients, the latter claim to produce improved results by partly accounting for the effects of pressure gradients and departure from equilibrium, which is a feature not supported in the standard wall functions. Given the complexity of the flow field induced by the irregular geometry of the shell, the non-equilibrium wall functions were adopted as the near wall treatment for the problem under study.

4. Boundary conditions

A crucial element in any CFD simulation is the definition of the environment surrounding the calculation domain. This environment is described by the boundary conditions, which can be specified by value or as functions of the dependent variables. The reliability of the simulation results greatly depends on the appropriate formulation of the boundary conditions and input values used in the calculation. An important topic of concern in wind engineering applications is the definition of the atmospheric boundary layer (ABL) profile in terms of velocity and turbulence characteristics. Assuming in this study a horizontally homogeneous turbulent ABL, meaning that properties are constant in directions tangential to the ground but can vary with the height, the

following velocity and turbulence property profiles (Eqs. (1)-(3)) were applied at the inlet of the 3D computational domain, as recommended by Richards and Hoxey (1993)

$$U(z) = \frac{u^*_{ABL}}{\kappa} \ln\left(\frac{z + z_0}{z_0}\right) \tag{1}$$

$$k(z) = \frac{u^{*2}_{ABL}}{\sqrt{C_\mu}} \tag{2}$$

$$\varepsilon(z) = \frac{u^{*3}_{ABL}}{\kappa(z + z_0)} \tag{3}$$

where z is the height co-ordinate, z_0 the roughness length, u^*_{ABL} the ABL friction velocity, κ the von Karman constant (0.40-0.42) and C_μ is a model constant of the standard k-ε model. These profiles, originally derived for the standard k-ε model, can also be used with other types of turbulence models, such as the RNG k-ε and Realizable turbulence models. When measurements of velocity, U, and turbulent kinetic energy, k (or turbulence intensity, which is a function of U and k), are not available, these profiles are a commonly used alternative in CFD simulations (Blocken *et al.* 2007). They are all based on the assumption that the height of the computational domain is significantly lower than the ABL height and, correspondingly, the shear stress remains approximately constant over the boundary layer and equal to the wall shear stress.

At the ground the non-slip boundary condition with a wall roughness height was applied. The standard rough wall-function model was used for this purpose. To ensure coherence between the turbulent law of the wall modified for mechanical roughness and the ABL log-law based on roughness length, Blocken *et al.* (2007) proposed for FLUENT the following relationship between sand-grain roughness height k_s and wind flow aerodynamic roughness length z_0

$$k_s \approx \frac{E}{C_s} z_0 = \frac{9.793}{C_s} z_0 \tag{4}$$

where $0 \le C_s \le 1$ is the roughness constant of wall function and $E \approx 9.793$ is the empirical constant for a smooth wall. In addition, to be consistent with physical arguments, the distance (z_p) from the center point (P) of wall-adjacent cell to the bottom wall of the domain should be kept larger than the sand-grain roughness height (k_s), that is, the condition $z_p > k_s$ shall be applied at the bottom of the calculation domain. Nevertheless, the combination of this condition with the constraint of Eq. (4) usually leads to distances of the center point (P) too high to obtain a good resolution of the flow near the ground. This problem can be circumvented if the requirement of limiting C_s to 1 is ignored (Gorlé *et al.* 2009) and a higher value is defined through a user defined function (UDF) on FLUENT. This was the procedure followed in this paper to define the ground boundary condition.

At the downstream boundary, the pressure outlet boundary condition was applied. The pressure outlet condition requires a fixed value for the relative static (gauge) pressure at the outlet boundary. The pressure value was set to zero in all simulations, i.e., the atmospheric pressure was assumed at the downstream boundary of the computational domain. For all other flow quantities no constraint is enforced at the outlet, which is approximately reproduced through the discretization scheme by

extrapolating their values from the flow in the interior domain.

At the lateral sides of the domain symmetry boundary conditions were employed, which enforce parallel flow by forcing the velocity component normal to the boundary to vanish and also zero normal derivatives for all flow variables. This has limited influence on results if lateral boundaries are placed sufficiently far from the region of interest, which is the case.

Finally, at the top boundary the most obvious and employed solution is to specify a symmetry boundary condition. However, the zero gradient boundary condition at the top of the domain is clearly inconsistent with the type of inlet boundary adopted, in which a constant shear stress along the height is assumed. Alternative solutions are proposed to overcome this incoherence. One possible solution is to impose at the top of the domain the correspondent conditions of the inlet boundary profile for all variables. Nevertheless, this solution would not allow fluid to exit and re-enter the domain, a situation that can be unwanted in the regions with obstacles since artificial accelerations could occur if the top boundary is not far enough for the flow not to be disturbed there by the obstacle's presence. As such, the top boundary was subdivided into two parts, accordingly to the grid discretization: the central part (Fig. 3), where the symmetry boundary condition was applied; and the remaining part, along which the inlet boundary conditions that result for the domain height were extended.

5. Numerical simulation and model calibration: initial results

The procedure followed in this work for calibrating the CFD model is checking if certain conditions generally accepted as important to improve the confidence in the simulation results are met. The conditions that were considered are summarized as follows: a) the ABL velocity profile should maintain its shape from the inflow boundary until the domain region where the model is placed; the dimensionless wall distance Y^+ of the wall-adjacent cells should ideally be in the interval $30<Y^+<300$ (log-law region or fully turbulent portion of the boundary layer); a number of cells should fall in the log-law region to fully capture the turbulent boundary layer profile; computed results should be insensitive to grid resolution.

To test the sensitivity of the results to the grid resolution, 6 different mesh sizes were applied, with totals of, respectively, 200291 cells (Mesh 1), 213927 cells (Mesh 2), 219532 cells (Mesh 3), 247154 cells (Mesh 4), 905318 (Mesh 5), and 1420210 cells (Mesh 6).

Standard environment conditions regarding wind velocity profile and terrain roughness were used in the calibration process as well as in all other simulations performed in the present study. More specifically, the recommendations of Eurocode 1 in Part 1-4 (Eurocode 2007, Lopes *et al.* 2010), on wind action on structures, were followed to define the parameters required by Eqs. (1)-(3). By comparing Eq. (1) with the wind velocity log-law profile recommended in the Eurocode, it results for the ABL friction velocity of Eq. (1) the following relationship

$$u^*_{ABL} = 0.234 \cdot \kappa \cdot z_0^{0.07} U_b \tag{5}$$

where U_b is the basic wind velocity defined as a function of wind direction and time of year at 10 m above ground of terrain category II (open country terrain with low vegetation). Concerning roughness length, z_0, terrains are divided into four categories, with roughness lengths of 0.01 m, 0.05 m, 0.3 m and 1.0 m, respectively, where the lower value corresponds to a calm open sea surface and the higher one respects to a forest or an urban area with high building density (15% of

the surface covered with buildings with an average height exceeding 15 m). For the validation process and subsequent study, a terrain category II (z_0=0.05 m) and a friction velocity of 0.8 m/s (corresponding to U_b≈10 m/s) were considered.

To obtain correct simulation results, it is important that the ABL profile is preserved from the inlet of the domain until it reaches the obstacle (i.e., the shell structure). This assumption was tested for the 6 mesh sizes referred to above and they all proved to be effective, with differences in the wind velocity vertical profile completely irrelevant upstream of the obstacle. Fig. 4 shows the mean horizontal wind velocity *U(z)* at different locations in the computational domain (see Fig. 3).

As can be seen, the inlet velocity profile (*x*=-42 m) practically remains unchanged, as wanted, until reaches the central region of the domain (*x*=-15 m). The ABL profile is strongly changed by the shell structure at the central region (*x*=0 m), as showed by a sudden decrease, followed by a rapid increase, of the velocity at the shell surface level. After overcoming the obstacle, the wind goes on its way in the downstream region with a profile that gradually tends to regain its original shape (*x*=50 m; *x*=118 m).

To inspect the adequacy of using the wall-function approach instead of resolving the flow all the way to the wall, the near-wall profiles of Y^+ were checked for the outer and inner shell surfaces. Fig. 5 shows the Y^+ values along the central *x*-line on the inner shell surface, and Fig. 6 shows the percent frequency distribution of the Y^+ values for the totality of each shell surface and grouped in selected ranges.

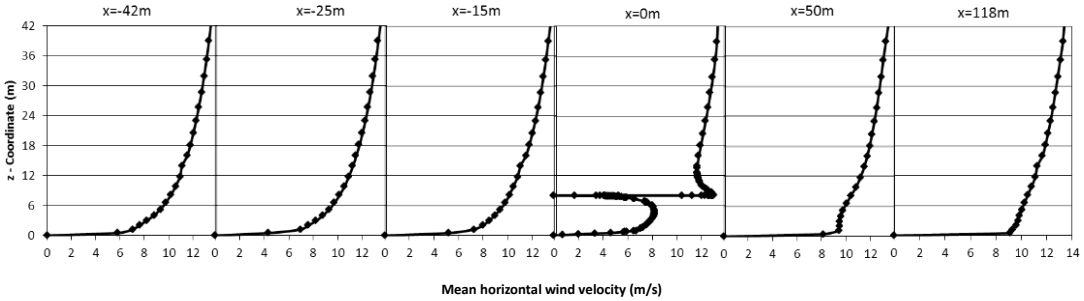

Fig. 4 Velocity magnitude profiles for *y*=0 m and variable *x* (Fig. 3)

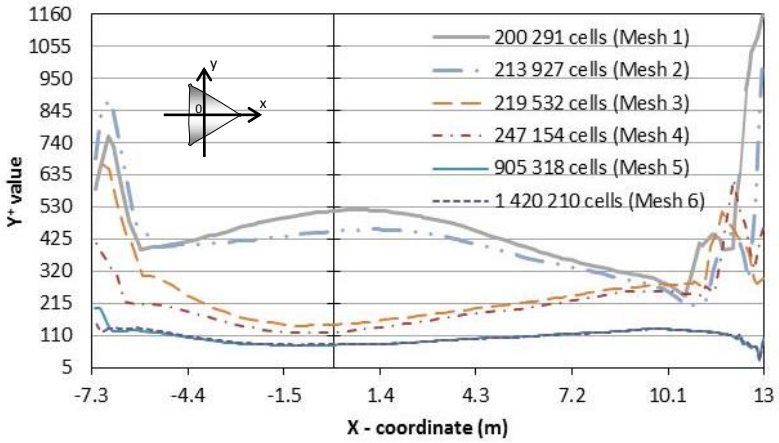

Fig. 5 Y^+ profiles on the inner shell surface along the central *x*-line

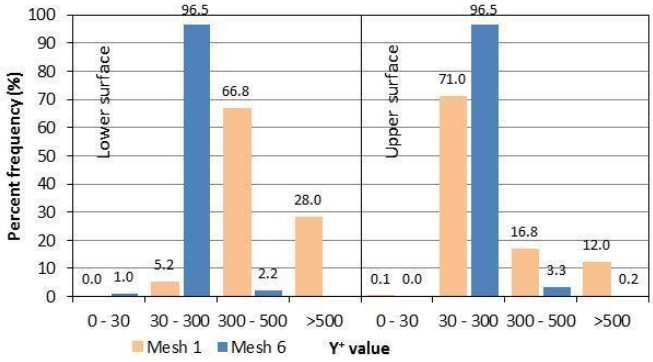

Fig. 6 Percent frequency distribution of Y^+ on the shell surfaces

As seen in Fig. 5, the Y^+ profiles that result for the various mesh sizes show visible differences between them but a convergence behaviour is clearly noticed as the number of cells increases. The highest Y^+ values are attained in the close vicinity of the shell edges, after which a rapid decrease occurs towards a more stable profile of lower Y^+ values. Mesh 5 and Mesh 6 pratically provide coincident Y^+ values and in both cases within the ideal range ($30<Y^+<300$) over the entire length of the central x-line. This suggests that grid independent results are achieved with 10^6 cells as order of magnitude. The percent frequency histogram for the Y^+ values over the outer and inner entire shell surfaces (Fig. 6) also shows that Mesh 6, compared with Mesh 1, should guarantee a superior quality of the results since 97% of the Y^+ values, for both outer and inner surfaces, are concentrated in the range $30<Y^+<300$, as recommended for the log-law model.

Fig. 7 provides a view of the Y^+ profiles in the immediate vicinity of the outer and inner shell surfaces along the central x-line for Mesh 6. One can notice that, regarding the inner surface, two to three Y^+ layers are nearly integrally immersed into the log-law region, which is an important feature for a proper capture of the turbulent boundary layer. The log-law region of the outer surface contains fewer computational nodes – one to two Y^+ layers of nodes – when compared to that of the inner surface, but if the observation is extended up to $Y^+=500$, which is often considered the upper limit of the log-law region, more layers of nodes are found. It can also be observed that all nodes are positioned above $Y^+=30$, which is a premise of the law-of-the-wall model.

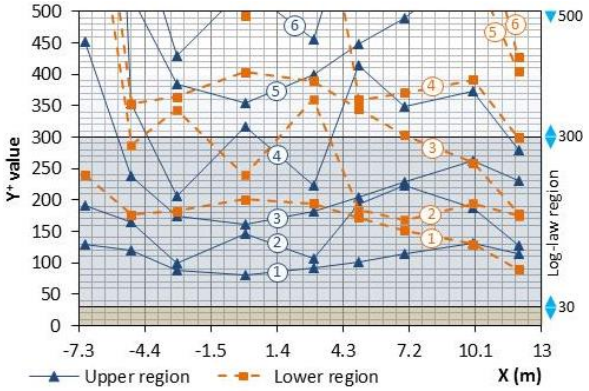

Fig. 7 Y^+ profiles along the central x-line

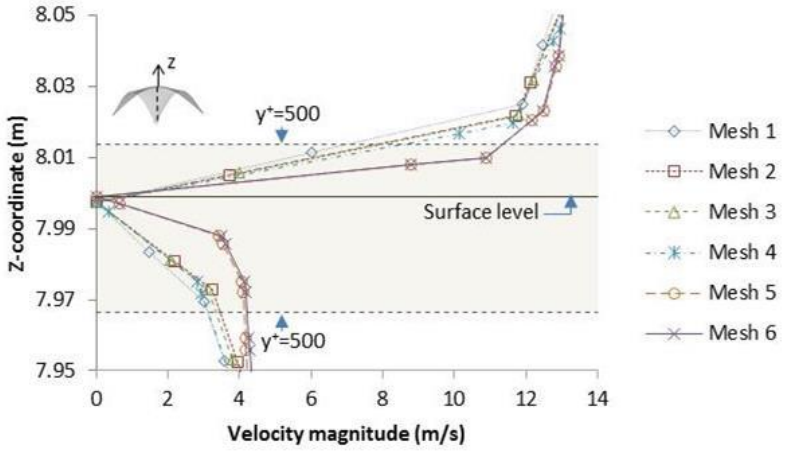

Fig. 8 Velocity magnitude in the vicinity of the point (0,0,*z*)

Fig. 8 shows the velocity magnitude profile along the *z*-axis in a region very close to the shell surface for all the mesh sizes referred to above. The showed chart allows perceiving the velocity gradients induced by the shell surfaces and the differences of the results yielded by the different mesh sizes. As anticipated by the Y^+ profiles of Fig. 5, the simulation results, in this case represented by the velocity magnitude, evidence a discernible difference between meshes 5 and 6 and the remaining ones. The profiles obtained confirm once more that grid independent results are attained from Mesh 5 onwards. Meshes 5 and 6, when compared to the other meshes, predict higher velocity gradients in the log-law region, after which results seem to converge for an identical solution for all the mesh sizes tested.

A finer resolution of the flow in the close vicinity of the shell surface is of capital importance for an accurate prediction of the wind loads and resultant structural design parameters. Therefore, the simulation results with Mesh 6 will be used in the next section for investigating the wind effects on the shell structure and providing data with possible use in the optimization of the shell design.

6. Wind action results and discussion

Wind loading can be considered as the most important external excitation, which acts almost permanently during the life of buildings and other structures. The effects of wind are of relevant importance to evaluate wind-induced natural ventilation of rooms and to assess wind loads on building components and structural systems. In the study at hand, the structural design is the problem under consideration, and the shape of the pressure distribution and the magnitude of the resultant forces that develop on the shell from the wind action are of primary importance for an efficient structural design. The wind effect can be decomposed into a static action (constant wind or slow variation in intensity) and a dynamic action (gusty wind, changes in direction). A correct assessment of the static action is of crucial importance, since dynamic effects of wind are usually assessed using equivalent quasi-static loads and dynamic amplification factors. The static action

exerted by the wind pressures on the shell are thoroughly described by the pressure coefficient distribution on the outer and inner shell surfaces. Moreover, the global forces that result from the surface pressure distribution resume the magnitude of the static wind loading and are of essential importance for a safe and proper design of the shell in terms of strength and mechanical stability. In the following sub-sections, the fundamental results concerning the wind pressure coefficients and resulting global forces are presented and discussed.

6.1 Pressure coefficients

The local pressure coefficient at a point on a surface is the ratio of the surface dynamic pressure on that point to the dynamic pressure in the upstream flow at a reference height. The calculation formula is as follows

$$C_p = \frac{p - p_\infty}{\frac{1}{2}\rho U_\infty^2} \tag{6}$$

where: p is the local surface dynamic pressure, p_∞ is the pressure of the free stream (pressure at some location where the flow is undisturbed by the shell structure) and U_∞ is the (upstream) velocity in the undisturbed flow at a reference height. In the present study, the reference height was set to the maximum shell height (z=8 m) and the undisturbed flow velocity at that height was computed from the inlet velocity boundary profile (U_∞=10.2 m/s).

Given the three-sided spatial geometry and central z-axis symmetry, only two directions of wind incidence are sufficient to fully represent the wind action on the shell. Figs. 9 and 10 show the pressure coefficient contours for the outer and the inner surface of the shell for incident wind directions of 0º and 60º, respectively.

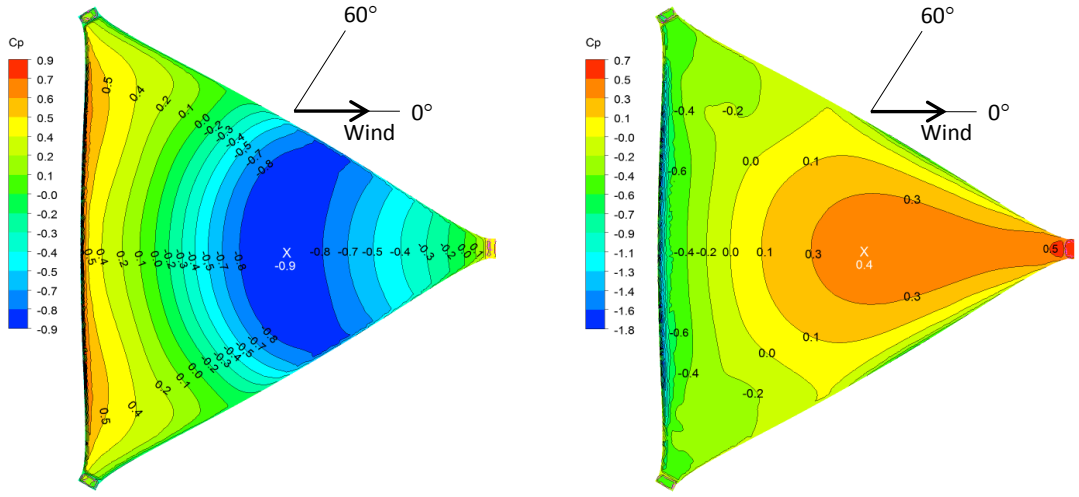

(a) Outer shell surface (b) Inner shell surface

Fig. 9 Pressure coefficient contours for a wind incidence angle of 0º (horizontal direction)

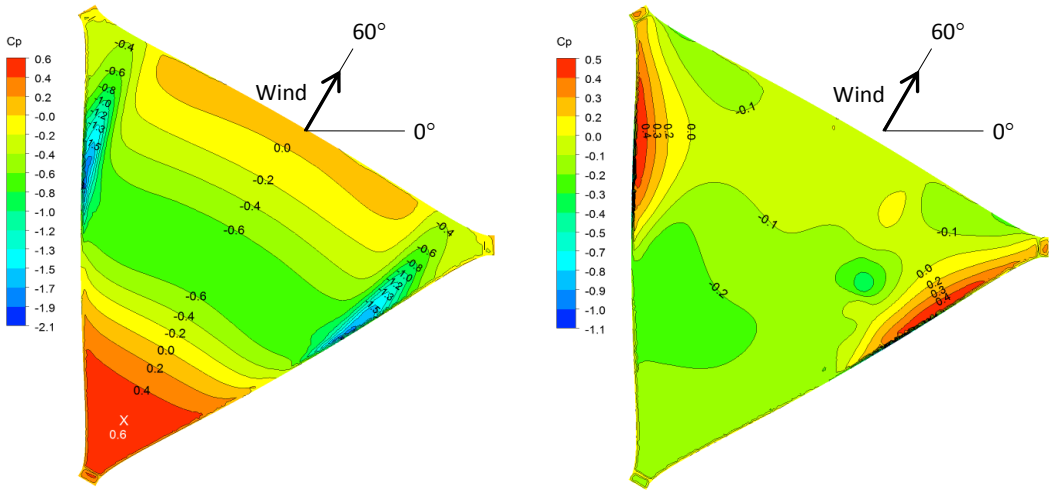

(a) Outer shell surface (b) Inner shell surface

Fig. 10 Pressure coefficient contours for a wind incidence angle of 60°

Starting with the case of 0° incidence angle, Fig. 9 shows that higher positive values of the pressure coefficient occur on a narrow band of the upstream border of the outer surface (Fig. 9(a)), where the flow first hits the shell, and on the inner surface of the downstream shell leg, as a result of the impingement of the flow on that surface (Fig. 9(b)). On the opposite side, the lower negative values occur on the same narrow upstream band of the higher values, but in this case on the inner surface (Fig. 9(b)), and on the outer surface of the shell, close to the region of maximum curvature (Fig. 9(a)).

For the case of 60° incidence angle, the higher positive pressure coefficients are observed on the outer surface of the shell leg that lies frontally to the flow (Fig. 10(a)), after which values decrease and are negative on two equal shaped side bands symmetrically positioned to the flow direction. In turn, the inner shell surface is mostly under negative pressure, with the exception of two side bands with positive pressure coefficients extending over approximately the same regions of the negative pressure bands of the outer surface.

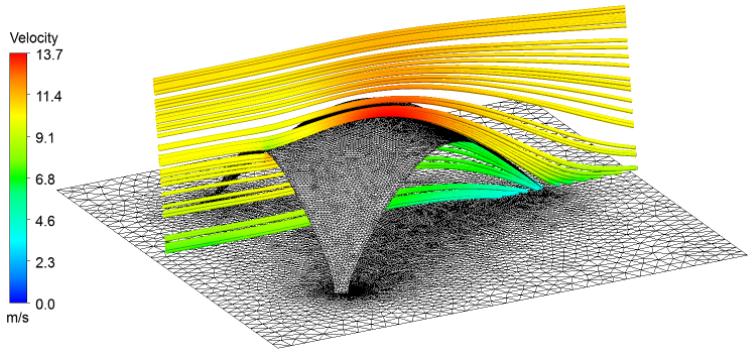

Fig. 11 Velocity magnitude streamlines on the 0° wind incidence plane (*yz* plane)

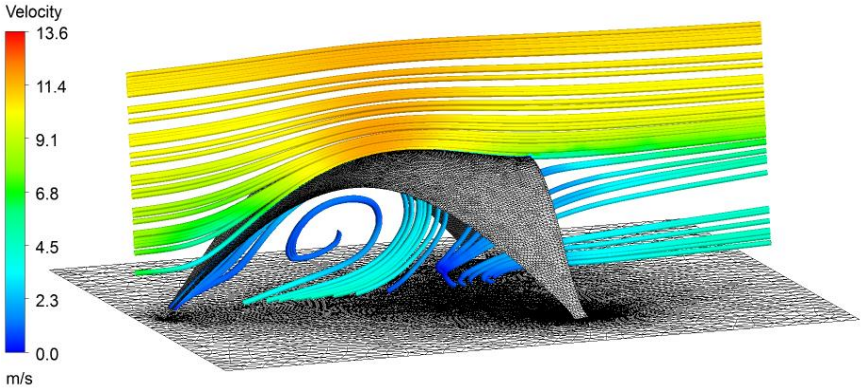

Fig. 12 Velocity magnitude streamlines on the 60º wind incidence plane

For a more comprehensive understanding of the pressure contours maps of Figs. 9 and 10, the velocity magnitude streamlines on the 0º and 60º wind incidence planes are represented in Figs. 11 and 12, respectively.

For the case of 0º incidence angle it is visible from Fig. 11 that streamlines get closer together when the fluid passes over the convex side of the shell. As the streamlines converge the velocity increases (Fig. 11) and, by Bernoulli's theorem, the pressure must decrease, which is consistent with the pressure coefficient distribution of Fig. 9(a). On the other hand, in the region under the shell (concave side), as the flow approaches the downstream supporting leg of the shell, the fluid slows down (Fig. 11) and the pressure increases, which Fig. 9(b) also evidences.

For the case of 60º incidence angle, comments similar to those made above are applicable. Fig. 12 shows that the airflow, after impinging upon the upstream leg of the shell, regains velocity and at the same time the pressure (coefficient) on the outer shell surface decreases, reaching its minimum negative value at the top of the shell (Fig. 10(a)). Meanwhile, this case presents an additional feature not observed in the previous case. A remarkable recirculation zone with low airflow velocities forms under the shell, giving rise to a negative pressure (coefficient) field on mostly of the inner shell surface, as Fig. 10(b) shows. The shape and velocity of the flow under the shell play an important role in pedestrian comfort and therefore are design variables that, for reasons other than structural strength, should be also taken into account.

6.2 Global forces and characteristic coefficients

Other important results on the aerodynamic effects of wind on the shell are the drag and lift forces. The drag force is a force parallel to the wind direction and is calculated by integrating the pressure field (pressure drag) and the shear stress (shear drag) in the flow direction over the entire shell surfaces (outer and inner surfaces). The lift force is a force perpendicular to the wind direction and is calculated in a similar way to the drag force but in this case the integration is performed in the direction perpendicular to the flow. It is common to present the drag and lift forces in the form of drag and lift dimensionless coefficients (Eq. (7)), which can be calculated from the respective forces by normalizing them with corresponding reference forces defined as the far-field dynamic pressure acting on a relevant plane area taken as reference, i.e.

Table 1 Drag and lift caused by wind flow

Direction	Drag			Lift		
	A (m^2)	F_D (N)	C_D (-)	A (m^2)	F_L (N)	C_L (-)
0º	304.5	3198.6	0.17	304.5	2523.9	0.13
60º	304.5	2112.2	0.11	304.5	3843.0	0.20

$$C_D = \frac{2F_D}{A \cdot \rho U_\infty^2} \quad C_L = \frac{2F_L}{A \cdot \rho U_\infty^2} \tag{7}$$

where U_∞ is a reference velocity of the far-field flow (the same velocity of Eq. (6)) and for the reference area (A) the planform area of the shell is adopted, i.e., the area projected on a plane parallel to the direction of flow and normal to the lift force.

In Table 1 the results for the drag and lift forces (F_D and F_L) and respective dimensionless coefficients are presented for the wind incidence angles of 0º and 60º and a reference velocity of U_∞=10.2 m/s.

Table 1 shows that the force in the direction of wind is higher for 0º incidence angle but in the case of the lift force the contrary is observed, with the 60º incidence angle being the critical direction. The drag and lift dimensionless coefficients reflect the relative magnitude of the different forces. The use of these dimensionless coefficients instead of the dimensional forces is useful when the purpose is the validation of experimental data or the comparison of different designs.

7. Conclusions

Thin and complex-shaped shells are becoming increasingly popular today as artistic expressions of modern architecture and/or special constructions with specific functionalities. The structural and mechanical stability of these elements, given their characteristics of slenderness and non-orthogonality, is a matter that deserves special attention by designers.

In this paper, the effect of wind on a free-form complex thin shell was analysed via 3D-CFD simulations. A hybrid structured-unstructured grid and the RNG k-ε turbulence model with non-equilibrium wall functions were employed in the computations. The model was calibrated in terms of mesh resolution by taking into consideration, among other aspects, the wall distance of the wall-adjacent cells and the grid independency of results. Some fundamental results were then obtained with interest for the structural design and mechanical stability of the shell: the wind pressure coefficient distribution on the outer and the inner shell surface, the global forces that result from the wind action, in the directions parallel and perpendicular to the flow, and the respective dimensionless characteristic coefficients.

Two wind incidence directions for the same characteristic inlet profile were analysed in this study: 0º and 60º incidence angle. The outer and inner surfaces showed pressure distributions, with

alternate positive and negative (suction) values, different from each other and between wind incidence directions. Regarding the magnitude of the loading imposed on the shell by the wind, the 0^{o} incidence angle has revealed as being the critical direction for the along-wind force while the 60^{o} incidence angle was the wind direction that induced the lift force of higher magnitude.

Wind-tunnel tests will always be important to create a more real picture of the dynamics of wind on structures, especially in case of complex shapes. Nevertheless, the rapid advances in CFD algorithms, computing power and visual graphics on computers, make the CFD technique a powerful alternative to wind-tunnel tests provided that it is used judiciously and the results produced cautiously interpreted. This paper represented a contribution towards the use of this technique on complex-shaped structures and provided results for the case of a free-form shell with possible utility in future confrontation with experimental results on the same or similar geometries.

Acknowledgements

The authors would like to thank the Institute for Plasmas and Nuclear Fusion (IPFN) at Instituto Superior Técnico (IST) for the use of ANSYS Fluent software. The authors would also like to acknowledge ICIST-CEris Research Center and Professors I. Vizotto and E. Júlio for the collaboration in the conception of the shell.

References

Adriaenssens, S., Block, P., Veenendaal, D. and Williams, C. (2014), *Shell Structures for Architecture: Form Finding and optimization*, (1st Ed.), Routledge, London.

Amin, J.A. and Ahuja, A.K. (2011), "Experimental study of wind-induced pressures on buildings of various geometries", *Eng. Sci. Technol. Int. J.*, **3**, 1-19.

ANSYS Fluent (2012), ANSYS Fluent Release 14.5, Theory Guide, ANSYS Inc., U.S.A.

Baskaran, A. and Kashef, A. (1996), "Investigation of air flow around buildings using computational fluid dynamics techniques", *J. Struct. Eng. - ASCE*, **18** (11), 861-873.

Behrouzi, F., Sidik, N.A.C., Nakisa, M. and Witri, A. (2013), "Numerical prediction of wind flow around the high-rise buildings by two equations turbulence models for urban street canyon", *Proceedings of the 15th International Conference on Mathematical and Computational Methods in Science and Engineering (MACMESE '13)*, Kuala Lumpur, Malaysia, April.

Bienkiewicz, B. and Sun, Y. (1992), "Local wind loading on the roof of a low-rise building", *J. Wind. Eng. Ind. Aerod.*, **45**, 11-24.

Blocken, B., Stathopoulos, T., Carmeliet, J. and Hensen, J.L.M. (2011), "Application of computational fluid dynamics in building performance simulation for the outdoor environment: an overview", *J. Build. Perform. Simul.*, **4**(2), 157-184.

Blocken, B., Stathopoulos, T. and Carmeliet, J. (2007), "CFD simulation of the atmospheric boundary layer-wall function problems", *Atmos. Environ.*, **41**, 238-252.

Eurocode (2007), Actions on Structures. Part 1-4: General actions-Wind actions, European Committee for Standardization, Brussels, Belgium.

Evola, G. and Popov, V. (2006), "Computational analysis of wind driven natural ventilation in buildings", *Energy Build.*, **38**, 491-501.

Franke, J., Hellsten, A., Schlnzen, H. and Carissimo, B. (2007), "Best practice guideline for the CFD simulation of flows in the urban environment", COST Action 732: Quality assurance and improvement of microscale meteorological models, University of Hamburg Meteorological Institute, Hamburg.

Gomes, M.G., Moret Rodrigues, A. and Mendes, P. (2005), "Experimental and numerical study of wind pressures on irregular-plan shapes", *J. Wind Eng. Ind. Aerod.*, **93**, 741-756.

Gorlé, C., van Beeck, J., Rambaud, P. and Van Tendeloo, G. (2009), "CFD modelling of small particle dispersion: The influence of the turbulence kinetic energy in the atmospheric boundary layer", *Atmos. Environ.*, **43**, 673-681.

Irtaza, H., Beale, R.G., Godley, M.H.R. and Jameel, A. (2013), "Comparison of wind pressure measurements on Silsoe experimental building from full-scale observation, wind-tunnel experiments and various CFD techniques", *Int. J. Eng. Sci. Technol.*, **5**, 28-41.

Lateb, M., Masson, C., Stathopoulos, T. and Bédard, C. (2010), "Influence of turbulence models on pollutant dispersion studies around a building complex", *Proceedings of the 5th International Symposium on Computational Wind Engineering (CWE2010)*, Chapel Hill, North Carolina, USA, May.

Liu, C., Leung, D.Y.C., Man, A.C.S. and Chan, P.W. (2010), "Computational fluid dynamics simulation of the wind flow over an airport terminal building", *Appl. Phys. Eng.*, **11**(6), 389-401.

Liu, X., Niu, J. and Kwok, K.C.S. (2013), "Evaluation of RANS turbulence models for simulating wind-induced mean pressures and dispersions around a complex-shaped high-rise building", *Build. Simul.*, **6**, 151-164.

Lopes, M.F.P., Paixão Conde, J.M., Gomes, M.G. and Ferreira, J.G. (2010), "Numerical calculation of the wind action on buildings using Eurocode 1 atmospheric boundary layer velocity profiles", *Wind Struct.*, **13** (6), 487-498.

McNeel R. and Associates (2003), Rhinoceros user guide: NURBS modeling for Windows: Version 3.0, Robert McNeel & Associates, Seattle, Washington, USA.

Montazeri, H. and Blocken, B. (2013), "CFD simulation of wind-induced pressure coefficients on buildings with and without balconies: validation and sensitivity analysis", *Build. Environ.*, **60**, 137-149.

Murakami, S. and Mochida, A. (1988), "3-D numerical simulation of air flow around a cubic model by means of the k-ε model", *J. Wind Eng. Ind. Aerod.*, **31**, 283-303.

Peterka, J.A. (1983), "Selection of local peak pressure coefficients for wind tunnel studies of building", *J. Wind Eng. Ind. Aerod.*, **13**, 477-488.

Richards, P.J. and Hoxey, R.P. (1993), "Appropriate boundary conditions for computational wind engineering models using the k-ε turbulence model", *J. Wind Eng. Ind. Aerod.*, **46-47**, 145-153.

Rogers, H. (2009), "Structural form in History and the construction of complex forms", *Proceedings of 3rd International Congress on Construction History*, Brandenburg, Germany, May.

Tomé, A., Vizotto, I. and Eduardo, J. (2014), "Guidelines for supporting the production of concrete shells scale models for wind tunnel aerodynamic studies", *5as Jornadas Portuguesas de Engenharia de Estruturas (JPEE)*, Lisbon, Portugal, November (in Portuguese).

Vizotto, I. and Ferreira, A.M. (2015), "Wind force coefficients on hexagonal free form shell", *Eng. Struct.*, **83**, 17-29.

Yakhot, V., Orszag, S.A., Thangam, S., Gatski, T.B. and Speziale, C.G. (1992), "Development of turbulence models for shear flows by a double expansion technique", *Phys. Fluids.*, **4**, 1510-1520.

Yazid, A.W.M., Sidik, N.A.C., Salim, S.M. and Yusoff, N.H.M. (2013), "Numerical prediction of air flow within street canyons based on different two-equation k-ε models", *Proceedings of the 2nd International Conference on Mechanical Engineering Research (ICMER2013)*, Pahang, Malaysia, July.

Zisis, I. and Stathopoulos, T. (2009), "Wind tunnel experiments on a patio cover attached to a low-rise building", *Proceedings of the 11th Americas Conference on Wind Engineering*, San Juan, Puerto Rico, June.